Research in Astronomy and Astrophysics, 24:045016 (9pp), 2024 April https://doi.org/10.1088/1674-4527/ad349a

Weak Merging Scenario of CLASH Cluster A209

Wen-Cheng Feng[1,2], Heng Yu[3], Hai-Hui Zhao[1], Xiao-Lan Hou[3], Shu-Mei Jia[2], Cheng-Kui Li[2], Yu-Lin Cheng[4], Paolo Tozzi[5], Ming Sun[6], and Yong Chen[2]
[1] Department of Physics and Institute of Theoretical Physics, Nanjing Normal University, Nanjing 210023, China; fengwc@njnu.edu.cn, zhaohh@njnu.edu.cn
[2] Key Laboratory of Particle Astrophysics, Institute of High Energy Physics, Chinese Academy of Sciences, Beijing 100049, China
[3] Department of Astronomy, Beijing Normal University, Beijing 100875, China; yuheng@bnu.edu.cn
[4] Department of Astronomy, Yunnan University, Kunming 650091, China
[5] INAF—Osservatorio Astrofisico di Arcetri, Largo E. Fermi, 50122 Firenze, Italy
[6] Department of Astronomy, University of Virginia, P.O. Box 400325, Charlottesville, VA 22904-4325, USA
Received 2023 October 31; revised 2024 March 5; accepted 2024 March 12; published 2024 April 10

Abstract

We study the structural and dynamical properties of A209 based on Chandra and XMM-Newton observations. We obtain detailed temperature, pressure, and entropy maps with the contour binning method, and find a hot region in the NW direction. The X-ray brightness residual map and corresponding temperature profiles reveal a possible shock front in the NW direction and a cold front feature in the SE direction. Combined with the galaxy luminosity density map we propose a weak merger scenario. A young sub-cluster passing from the SE to NW direction could explain the optical subpeak, the intracluster medium temperature map, the X-ray surface brightness excess, and the X-ray peak offset together.

Key words: X-rays: galaxies: clusters – galaxies: clusters: intracluster medium – galaxies: clusters: Abell 209

1. Introduction

Galaxy clusters are the largest gravitational bound systems in the Universe, reaching virial masses of $10^{14}M_{\odot}$–$10^{15.5}M_{\odot}$. They are usually located at knots of the cosmic web, and are affected by the surrounding large-scale structure. They continuously grow up by accreting diffuse matter, field galaxies, and merging galaxy groups (Kravtsov & Borgani 2012; Vikhlinin et al. 2014; Lyskova et al. 2019). Merging galaxy clusters are ideal astrophysical laboratories for studying hydrodynamic processes such as shock waves, turbulence, and particle acceleration.

During the merging process, different cluster components show different behaviors. Dark matter halos and galaxies, as collisionless particles (Clowe et al. 2006), are only affected by gravity. While the dominant baryon component—intracluster medium (ICM) is shaped by gravity and pressure, and also affected by viscosity and magnetic fields (Merten et al. 2011). Studying the dynamics of galaxies and diffuse hot baryons provides a wealth of information about the nature of dark matter, the dynamical state of the cluster, and the physics of the ICM. When the collision among halos is not head-on, the central region of the host cluster may show several peculiar signatures. In particular, the gas in the core will begin sloshing, and the brightest central galaxy (BCG) may show an offset up to tens to hundreds of kpc with respect to the centroid of the X-ray emission from the ICM (Dawson et al. 2012; Menanteau et al. 2012; Seppi et al. 2023). The amplitude of the projected offset between the BCG position and the X-ray peak could be used to identify major mergers in clusters (Mann & Ebeling 2012; Rossetti et al. 2016).

A209 is a massive galaxy cluster at a medium redshift ($z = 0.209$) with a high X-ray luminosity of $1.4 \times 10^{45}\ h_{70}^{-2}\ \mathrm{erg\ s^{-1}}$ (Ebeling et al. 1996). It is included in the Cluster Lensing And Supernovae survey with Hubble (CLASH)[7] sample. CLASH is a 524-orbit Multi-Cycle Treasury Program to accurately constrain the mass distributions of 25 galaxy clusters with their gravitational lensing properties (Postman et al. 2012). As a CLASH cluster, A209 has quite abundant multi-band joint observations, e.g., 20 orbits of HST observation, one hour VLA observation, five bands Subaru images, 2543 VLT spectra, 31 ks Spitzer observation etc. (see Postman et al. 2012, for more details).

A209 has not relaxed. Mercurio et al. (2003a) showed a relevant evidence of substructure and dynamical segregation with optical data. With the study of the optical luminosity functions of A209, Mercurio et al. (2003b) also found faint galaxies of A209 need additional Schechter components to be fitted. The color distribution of galaxies shows clear asymmetry. The reddest region of A209 is around the center and extends in the southeast–northwest (SE–NW) direction (Haines et al. 2004). Similar structures can be found in the weak lensing mass, with an elongated structure extending in the same direction (Haines et al. 2004; Paulin-Henriksson et al. 2007). Smith et al. (2005) suggests this system is marginally unrelaxed

[7] https://archive.stsci.edu/prepds/clash/

Table 1
Basic Information of Observations of Chandra and XMM-Newton

obsID	Instrument	Start Data	Exp (ks)	Clean Exp (ks)
Chandra				
522	ACIS-I	2000-09-09	9.96	9.02
3579	ACIS-I	2003-08-03	9.99	8.78
XMM-Newton				
0084230301	PN/MOS	2001-01-15	14.16/20.05	12/17

based on a mass ratio between the cluster main component and the total mass (both at $r < 500$ kpc). (Maughan et al. 2008) derived an ellipticity of 0.21 ± 0.01 for this cluster. Moreover, as temperature drop is less than 30% of the peak temperature toward the cluster center (Zhang et al. 2007), and the luminosity within $0.05r_{500}$ is less than 0.17 times the total luminosity within r_{500} (Sayers et al. 2013; Shitanishi et al. 2018), A209 is classified as a non-cool-core cluster in the X-ray band, and its optical center is not overlapping with its X-ray peak, with a projected offset distance of 14 kpc (Yu et al. 2018).

In the radio band, an extended halo in A209 is detected with the VLA at 1.4 GHz of A209 (Giovannini et al. 2006), and later with the 610 MHz GMRT data by Venturi et al. (2007). Besides, a spectacular radio halo revealed by the *MeerKAT* at the *L*-band (900–1670 MHz) recently extends to at least 4.′2 radius (or 0.85 Mpc) from the center (Knowles et al. 2022). This is a sign of past AGN activities or merging events.

In this work, we study the gas morphology and structure of A209 with the observations of Chandra and XMM-Newton, combining with the optical data to reveal its dynamical status. This paper is arranged as follows: X-ray and optical data analysis is described in Section 2, while the results of data analysis are presented in Section 3. In Sections 4 and 5, we discuss our results and draw conclusions. In this work, $H_0 = 67.4\ \mathrm{km\ s^{-1}\ Mpc^{-1}}$, $\Omega_m = 0.315$, $\Omega_\Lambda = 0.680$ (Planck Collaboration et al. 2021). The physical scale of $1'' = 3.346$ kpc at the redshift of A209.

2. Data and Analysis

2.1. X-Ray Data

A209 was observed by Chandra on 2000 September 9 for 9.96 ks (obsID 522) and on 2003 August 3 for 9.99 ks (obsID 3279). Both observations were carried out using the Advanced CCD Imaging Spectrometer (ACIS-I) in the VFAINT mode. The cluster was also observed by XMM-Newton on 2001 January 15 (obsID 0084230301) and covered on the observation of 2008 December 16 (obsID 0550960101). Because in the later observation A209 is located at the very edge of the field. We only adopt the first observation. The basic information of observations of Chandra and XMM-Newton is listed in Table 1.

We use standard software package CIAO (version 4.13) to analyze the Chandra data retrieved from the archive, `chandra_repro` script to reprocess each observation to obtain the events file. The high-energy background flare events are filtered out by `lc_clean` command and we obtain the good time (GTI) of 9.02 ks and 8.78 ks for these two observations, respectively. We use `merge_obs` to create combined exposure-corrected images. Point sources within the field of view (FOV) are identified by `wavdetect` on the Chandra 0.5–7 keV band image with a detection limit of two counts per pixel, corresponding to a flux limit of $10^{-15}\ \mathrm{erg\ cm^{-2}\ s^{-1}}$, checked visually and eventually masked. We select the background region away from the center of the cluster where the surface brightness declines to a flat level.

The XMM-Newton data reduction is carried out in the XMM-Newton Science Analysis System version 20.0.0. We use `epchain` and `emchain` to reduce events files and extract the light curve by `evselect`. We select the time range with no obvious light variations and remove the flare (the time period when the counts excess 3σ more than the mean level) from it. After cleaning, we obtain GTI of 12 ks for PN, and 17 ks for MOS1 and MOS2 respectively. We exclude point sources by visual check refer to the point source list of Chandra and choose the background at the edge of the field with the same standard used for Chandra data.

Figure 1 shows the XMM-Newton and combined Chandra exposure-corrected X-ray image of A209 in 0.5–7 keV band with the surface brightness contours from XMM-Newton as a reference. The BCG is located at R.A. $= 1^{\mathrm{h}}31^{\mathrm{m}}52^{\mathrm{s}}.55$, decl. $= -13°36'40''.49$ (J2000) (as shown with the green cross in Figure 1). The X-ray peak (the pixel with the highest count rate) is located at R.A. $= 1^{\mathrm{h}}31^{\mathrm{m}}52^{\mathrm{s}}.9$, decl. $= -13°36'41''.70$ (J2000) with an error of $0''.5$ (as shown with the blue cross in Figure 1). The projected offset between the BCG and X-ray peak is 17.5 ± 1.7 kpc. The X-ray emission of the entire galaxy cluster presents an elongated shape along SE–NW direction.

2.2. Optical Data

To investigate the spatial distribution of A209 member galaxies, we use photometric data to create a luminosity density map of galaxies in A209. The photometric data is from the CLASH project, observed by Subaru/SuprimeCam from

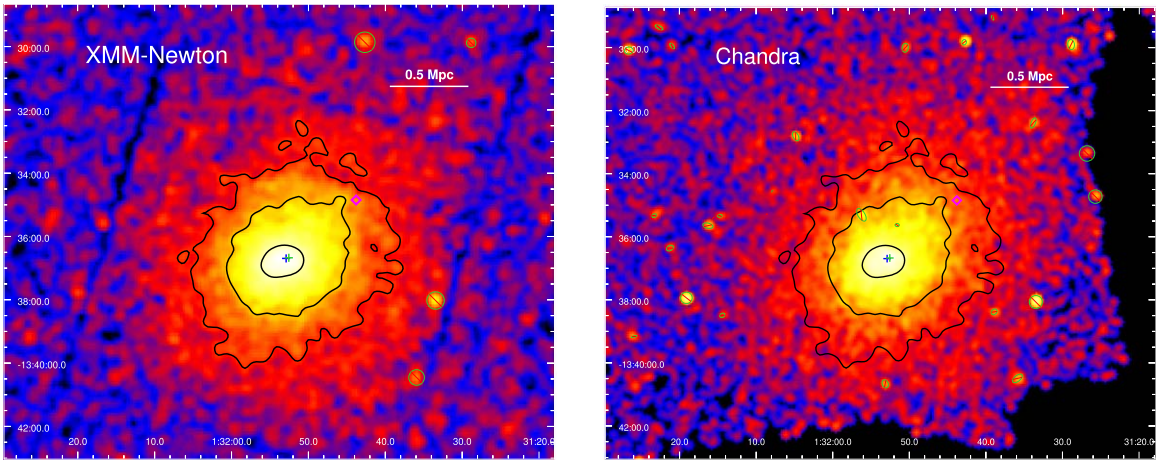

Figure 1. X-ray images of A209 with the same size and the same color scale in the 0.5–7.0 keV band from XMM-Newton MOS1 detector and the combined Chandra data, respectively. Both images are smoothed with a Gaussian of FWHM $= 0\farcs5$. These green elliptical areas represent point sources masked in further analysis. The black lines are surface brightness contours from XMM-Newton MOS1 detector. The green and blue crosses represent the position of BCG and the X-ray peak, respectively.

SMOKA (Baba et al. 2002). Based on Subaru's observational catalog, there are photometric data of 87,597 galaxies, covering a sky range of $22.65 < \mathrm{R.A.} < 23.30$, $-13.86 < \mathrm{decl.} < -13.33$, with a magnitude limit of 28.9 mag in R_C band. To examine the accuracy of the photometric redshift of the photometric data, we refer to the spectral data from CLASH-VLT (Annunziatella et al. 2016). The VLT observations have a total of 2653 spectroscopic data covering a sky range of $22.74 < \mathrm{R.A.} < 23.20$, $-13.80 < \mathrm{decl.} < -13.41$, with a magnitude limit of 27.8 mag in R_C band.

We cross-match the photometric catalog with the spectroscopic catalog, and the magnitude limitation of galaxies is $R_C = 20.5$. When the projected spatial distance of two galaxies is within $1''$, they are identified as the same galaxy. We finally obtained 565 galaxies with both photometric redshifts and spectroscopic redshifts.

From these cross-matched galaxies, we select 396 galaxies with photometric redshifts within 0.21 ± 0.05, and check their spectroscopic redshifts to validate the accuracy of the photometric redshifts. We find that the standard error σ of the photometric redshift deviation is 0.041. There are 346 galaxies having spectroscopic redshifts within 0.21 ± 0.02, accounting for 87.4% of the total sample. There are 317 galaxies of them with spectroscopic redshifts within 0.21 ± 0.01, accounting for 80.1%. Thus photometric redshifts for galaxies brighter than 20.5 mag $R_C < 20.5$ in this redshift bin $z = 0.21 \pm 0.05$ could be a valuable complement to spectral measurements.

To analyze the optical galaxy distribution of A209, we choose a $0.2^\circ \times 0.2^\circ$ FOV centered on A209 (R.A. $= 22.97$ and decl. $= -13.61$). There are 252 galaxies (241 spectroscopic redshifts and 11 photometric redshifts) within $z = 0.21 \pm 0.01$. The additional 11 photometric galaxies generally distribute uniformly in the field. We use these 252 galaxies to generate the luminosity density map.

The luminosity density map of galaxies is derived according to the method described by Wen & Han (2013). Our FOV is divided into 100×100 grids. The luminosity of each galaxy is calculated based on its redshift and magnitude, and smoothed with a 2D Gaussian window of $0\farcm5$ width. The total R_C band luminosity of each grid is contributions of all galaxies in the field. The peak and subpeak are determined according to the grid bins with the highest integrated luminosity. The result is shown as Figure 2.

Galaxy distribution is generally elongated in the NW-SE direction. It contains two mass concentrations. The densest one is close to the BCG (represented by a green cross). The center of the subpeak is at R.A. $= 22.9325$, decl. $= -13.5808$, represented with a purple diamond in Figure 2. It is about $2\farcm8$ away in the NW direction. It is reported as the highest galaxy number density by Annunziatella et al. (2016). This luminosity density map is consistent with the results obtained with red sequence galaxies by von der Linden et al. (2014). The subpeak indicates the existence of a sub-cluster.

The galaxies represented by the orange stars in Figure 2 are the top two galaxies next to BCG in brightness. None of the top ten brightest galaxies in the field is close to the subpeak region. Thus this sub-cluster is mainly composed of low-mass galaxies, lacking massive galaxies. This suggests that it might be a young group.

3. Analysis and Results

The elongated and asymmetric X-ray emission and the existence of an optical subpeak reflect there are perturbation processes inside the cluster. In order to reveal the

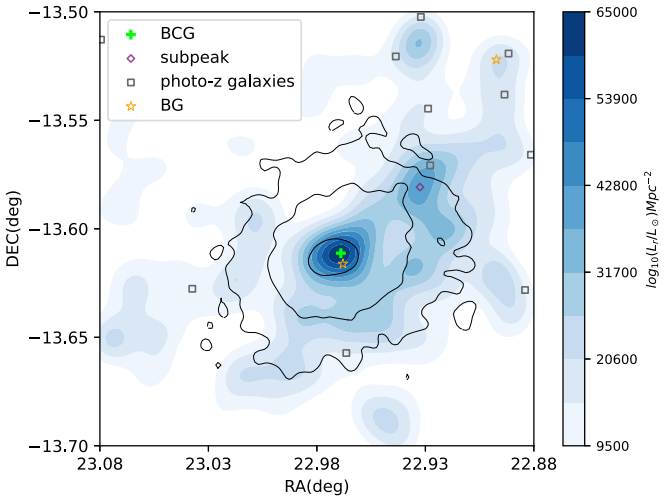

Figure 2. Galaxy luminosity density map generated with the Subaru photometric data (galaxies with r band magnitude $R_C < 20.5$, photometric redshift $z_{\rm phot}$ in the range of 0.209 ± 0.05) to show the NW-to-SE/E extension. The orange stars represent the two brightest galaxies (BG) apart from the the BCG. The purple diamond shows the region of subpeak. The gray square are galaxies with photometric redshift. The black line areas and green cross are same as above. Luminosity densities greater than 10,000 $\log_{10}(L_r/L_\odot)$ Mpc^{-2} are structures with more than three times the average luminosity density.

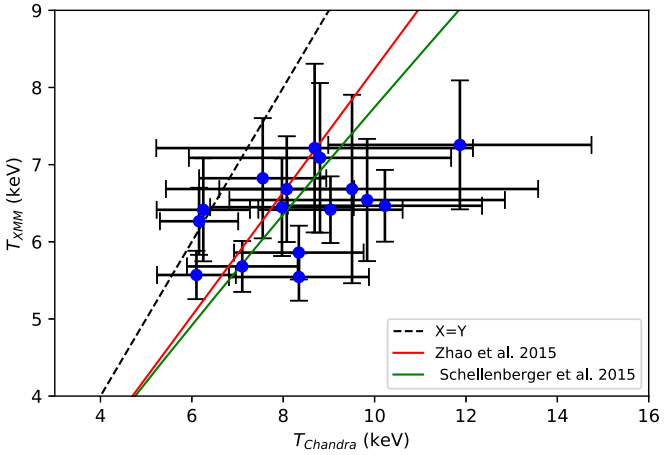

Figure 3. Temperature comparison between XMM-Newton and Chandra. The green and red lines in the figure represent the relation between the temperatures measured by XMM-Newton and Chandra data in Schellenberger et al. (2015) and Zhao et al. (2015), respectively.

thermodynamic properties and possible merger activity, we study the spectral characteristics of the hot gas in the cluster.

3.1. Spectral Fitting

We adopt the contour-binning software (Sanders 2006) to explore the spatial distribution of physical properties of A209. With a signal-to-noise ratio of 40, the software divides the cluster into 16 regions based on the surface brightness of combined exposure-corrected X-ray image observed by Chandra.

We use XSPEC (version 12.1.1) to fit the spectra extracted from Chandra data. The X-ray emission of A209 can be characterized by an absorbed APEC component from hot diffuse gas (Smith et al. 2001). We fit the spectra data in the energy band 0.5–7 keV with the model TBABS $*$ APEC. The galaxy neutral hydrogen column density is set to 1.43×10^{20} cm^{-2} and the redshift is fixed to 0.209. The metallicity, temperature and normalization are set free.

With the same 16 regions, we withdraw spectra from all three detectors of XMM-Newton—PN/MOS1/MOS2, and fit them simultaneously in the same way as mentioned above.

We compare the temperature values measured by the two telescopes in the same region as shown in Figure 3. The temperatures measured with Chandra are systematically higher than those measured with XMM-Newton. This trend is consistent with the relation revealed by previous studies (Schellenberger et al. 2015; Zhao et al. 2015).

3.2. Temperature, Pressure and Entropy Maps

The temperature maps and corresponding error maps obtained from XMM-Newton and Chandra data are shown in Figure 4. There is a hot region in the NW direction on both maps. It looks especially obvious in the Chandra image, although it has a relatively large error. To evaluate the temperature variation from the center toward the NW direction, we draw a line from the center to the northwest and plot the temperatures along the direction of the line. The result is shown in Figure 5. The ICM temperature is about 6 keV in the core region, generally increase to a peak at the radius of $\sim 1\farcm75$ in the NW direction, then drop outwards. Both Chandra and XMM-Newton results show similar trends. However the signal-to-noise is not very high due to large measurement errors.

This region is located between the core and the optical subpeak. To investigate its thermodynamic property, we study the pseudo-pressure and pseudo-entropy distributions. The thermal pressure and entropy can be defined as $P = kTn_e$ and $S = kTn_e^{-2/3}$ (Sasaki et al. 2016), n_e is electron density and kT is temperature. Since the normalization obtained by spectral fitting is proportional to the square of electron density, we convert P and S to $P \propto kT\mathrm{norm}^{0.5}$ and $S \propto kT\mathrm{norm}^{-1/3}$. The normalized pressure and entropy maps from XMM-Newton and Chandra are shown in the bottom left panel and bottom right panel of Figure 6, respectively. The hottest region in the NW direction also exhibits the largest pressure and the largest entropy. These evidences indicate there might be a shock front in this region.

3.3. The Brightness Residual Image

To verify the existence of the merger shock, we also check the surface brightness residual map of the cluster. Due to the

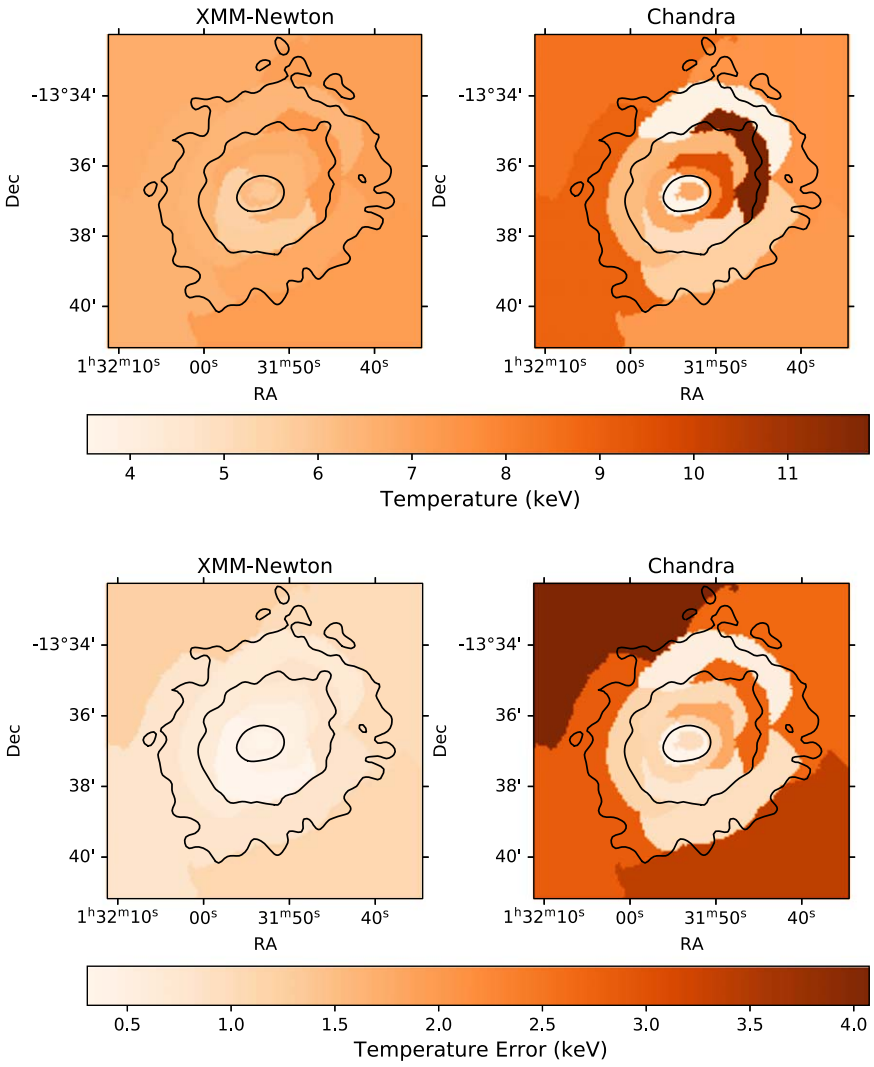

Figure 4. Temperature maps obtained from XMM-Newton and Chandra data with the contour-binning method. Top panel: gas temperature map; bottom panel: the temperature error map.

significant influence of bad channels on the XMM-Newton images of PN and MOS2, we only use the MOS1 detector to do the surface brightness fitting. Although its spatial resolution is lower than Chandra, the larger number of photons could give a better constrain on the general shape of possible excesses. The brightness residual image obtained by subtracting a classical double β elliptical model from the image is shown in Figure 7.

There are two areas with brightness exceeding in the NW and southeast (SE) directions, respectively. The diffuse arc-like brightness excess in the NW region overlaps with the high temperature region, just behind the optical subpeak (shown as a purple diamond in Figure 6). To check their physical properties more precisely, we draw two sector regions to extract surface brightness profiles (SBPs) (shown in Figure 7 labeled with NW and SE).

Each of the extracted SBPs is fitted with a broken power-law model (shown in the upper-left panel of Figure 8) to determine a possible density discontinuity across the selected region. We find a clear discontinuity in the SBP at $3\farcm05$ northwest of the BCG. This position is shown with a dashed line in Figure 8. In the SE direction, there is a gas density drop by a factor of 1.52 at a distance of $\sim 1\farcm8$ from the BCG (Figure 8, right panel).

4. Discussion

4.1. The Shock Front and Cold Front

In order to determine the origin of the discontinuity, we measured the gas properties before and after the discontinuity with both Chandra and it XMM-Newton data. The temperature profiles of the two sectors are shown in the bottom panel of

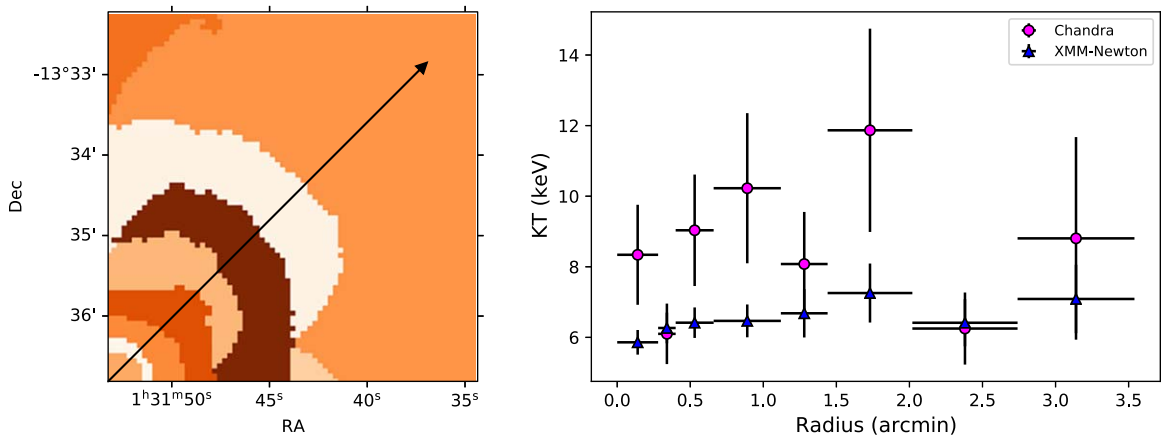

Figure 5. Left panel: the right upper quarter of the region captured by the contour-binning, where the temperature variation across the area traversed by the black solid line, represents our study on the temperature change from the center toward the NW direction. Right panel: the temperature of the region crossed by the black solid line in the left figure, with magenta dots and blue triangles representing measurements from Chandra and XMM-Newton data, respectively.

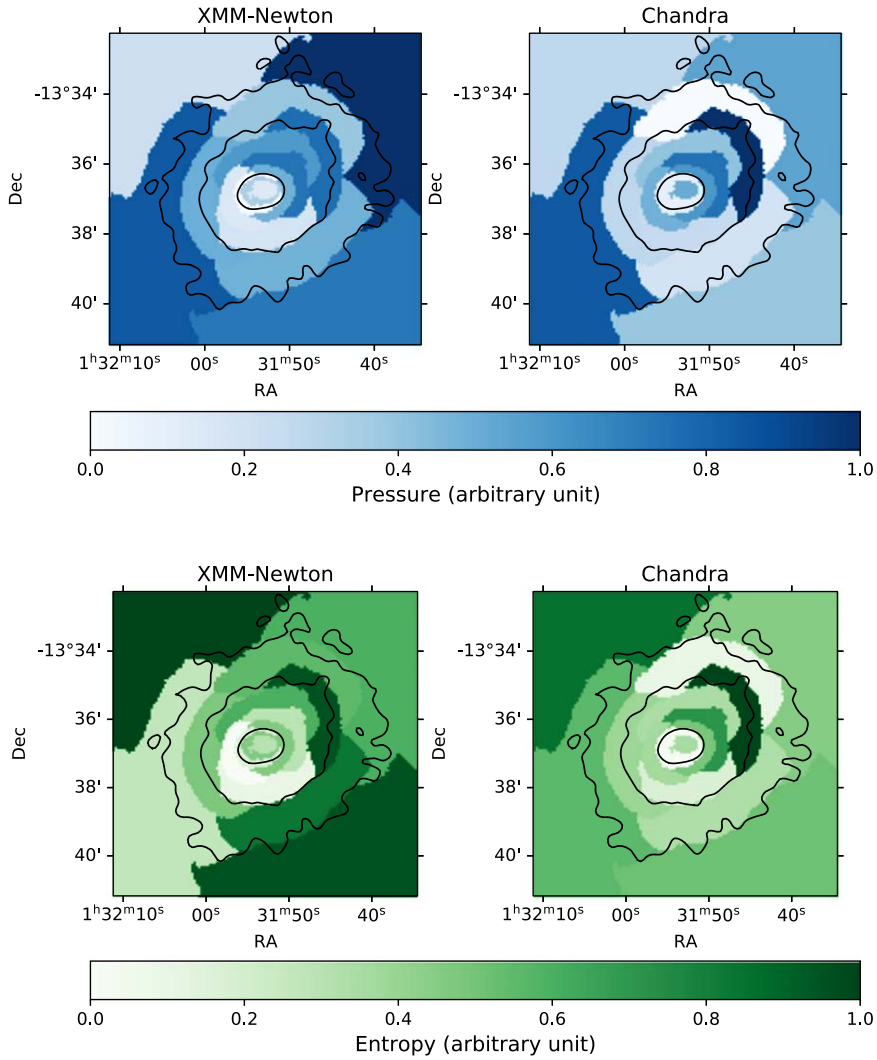

Figure 6. Pressure and entropy map obtained with the contour-binning method. bottom panel: gas pressure map with arbitrary unit; bottom panel: entropy map with arbitrary unit. Both the pressure map and entropy map have been normalized to represent their degree of variation and trend.

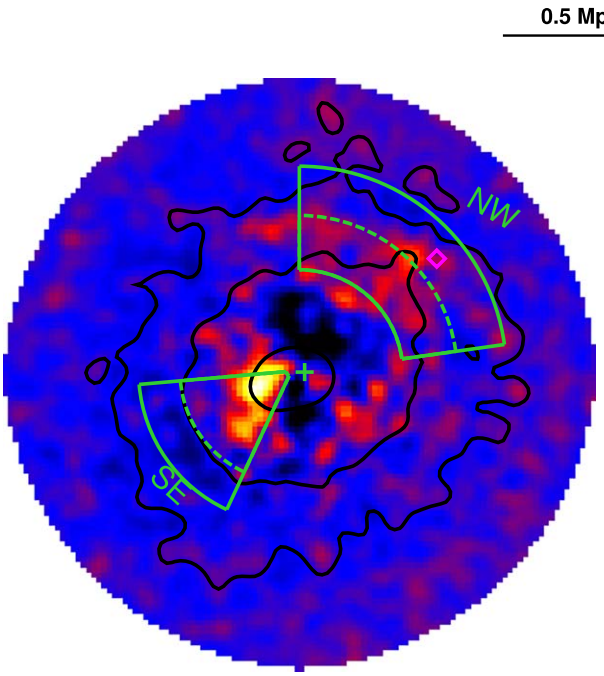

Figure 7. The smoothed XMM-Newton MOS2 surface brightness residual image. The black contours and green cross are the same as Figure 1. Two regions of interest in the SE and NW directions are made for surface brightness and temperature profiles shown in Figure 8. The dashed lines indicate the position of the X-ray discontinuity.

Figure 8. Both satellites show similar trends. Chandra data exhibit a strong jump signal in the NW direction.

We calculate the Mach number to study the possible shock heating. One way is based on the density discontinuity (Mirakhor et al. 2023):

$$\mathcal{M}_{\mathcal{C}} = \left[\frac{2C}{\gamma + 1 - C(\gamma - 1)}\right]^{\frac{1}{2}} \quad (1)$$

where the density compression factor $C = n_2/n_1$ is the ratio between the pre-shock density n_1 and the post-shock density n_2, γ is the specific heat ratio, assumed as $5/3$ (Sasaki et al. 2016). We could also derive the Mach number according to the temperature discontinuity

$$\mathcal{M}_{\mathcal{T}} = \left[\frac{(\gamma + 1)^2\left(\frac{T_2}{T_1} - 1\right)}{2\gamma(\gamma - 1)}\right]^{\frac{1}{2}} \quad (2)$$

where T_1 and T_2 are the pre-shock and post-shock temperatures at the location of the temperature discontinuity respectively.

For the surface brightness discontinuity in the NW direction, we obtain $C = 1.14$, corresponding to a Mach number of $\mathcal{M}_{\mathcal{C}} = 1.09^{+0.10}_{-0.06}$. This is almost the lower limit of the existence of a shock wave. At the same place, the Mach number derived with the XMM-Newton data is $\mathcal{M}_{\mathcal{T}} = 0.87^{+0.06}_{-0.07}$, which directly eliminates the possibility of a shock wave. In this case, the NW brightness exceeds is nothing more than a buildup of gas, caused by sloshing etc. On the other hand, the gas temperature of Chandra drops by a factor of $T_2/T_1 = 1.96$ (Figure 8, lower panel), resulting in a larger Mach number of $\mathcal{M}_{\mathcal{T}} = 1.76^{+0.19}_{-0.60}$. This supports the existence of a weak shock wave, which could be driven by the infalling young sub-cluster. Its immature core might have disintegrated in this merger. However, the error is too large to draw a solid conclusion.

While in the SE direction, the temperatures obtained by XMM-Newton and Chandra both show an increasing trend. No significant temperature jumps are seen around the discontinuity of surface brightness. Notably, this region has the lowest temperatures, pressure, and entropy (see Figures 4 and 6). The X-ray gas is offset slightly relative to the BCG in this same direction. Thus it is definitely not a counter shock, but likely to be a cold front caused by perturbations.

4.2. The Merging Scenario of CLASH Cluster A209

To put available pieces together, we propose a possible weak merger scenario as illustrated by Figure 9. A young sub-cluster without a BCG or a mature core fell into the main cluster from the SE direction. The gas of this sub-cluster is moving slightly faster than the local speed of sound, generating a weak shock wave in the interaction region. Its gas core was disrupted in the process, while its member galaxies keep propagating outwards in the NW direction. The gases on the path of the shock are heated, and the edge of arc-like brightness excess in the NW region corresponds to the position of shock front. Concurrently, the core gas of the primary cluster, disturbed by these dynamics, starts sloshing and forms a cold front in the southeast direction. The X-ray peak is also shifted in the same direction relative to the BCG.

5. Conclusions

A209 is an exciting and mysterious non-cool-core galaxy cluster with a clear asymmetry and an offset distance of 17.5 kpc between the X-ray centroid and the optical position. In this paper, we study the structural and dynamical features of A209 with X-ray observations and combine them with optical data. The main results of this work are summarized as follows:

(i) We create a luminosity density map of galaxies in A209 using optical data, which exhibits an elongated structure extending from SE to NW, with a subpeak $\sim 2\farcm80$ away from BCG in the NW direction.

(ii) With the contour binning method, we find that there is a region in the NW direction with the highest temperature and the largest pressure and entropy. The results from both XMM-Newton and Chandra data show similar trends. Their systematical differences are consistent with previous studies.

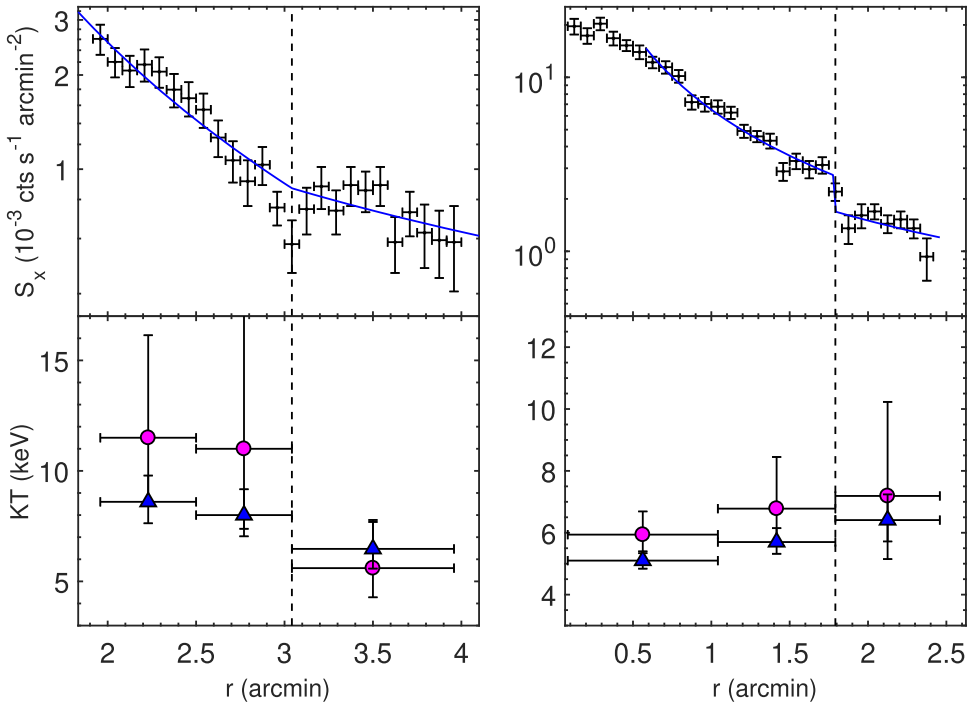

Figure 8. The surface brightness and temperature profiles for NW and SE regions shown in Figure 6. The blue solid line on the top panels are best fitting results of a broken-powerlaw model. The magenta circle points and blue triangle points on the bottom panels are from Chandra and XMM-Newton data, respectively. The black dashed lines indicate the X-ray discontinuity.

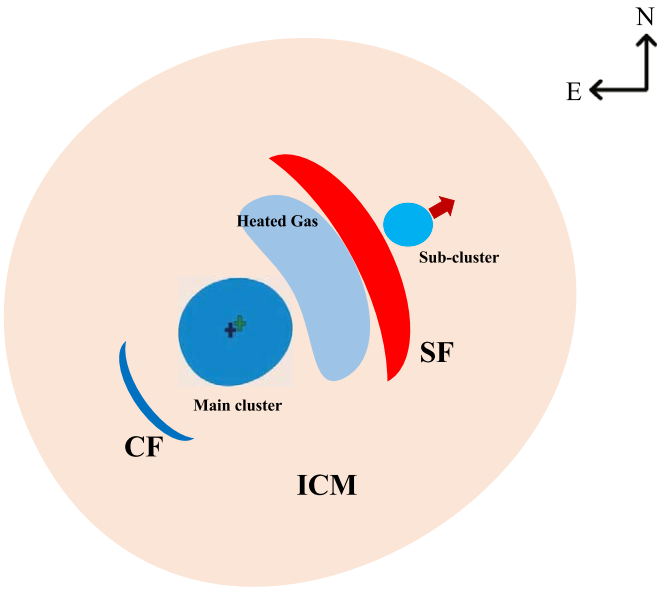

Figure 9. The illustration of the weak merger scenario of A209. A sub-cluster fall into the main cluster from the SE direction, then generate a shock wave in the NW direction and cause a cold front in the SE direction.

(iii) We analyze the brightness residual structure of A209 with XMM-Newton data, and extract the SBPs and temperature profiles from selected regions, revealing a possible weak shock front and a cold front feature in the NW and SE directions, respectively.

Combining all available observational evidences: the optical subpeak, the X-ray temperature map, the X-ray surface brightness excess, and the X-ray peak offset, we suggest that A209 is undergoing a weak merger. Due to limited exposure time of X-ray data, many details of the merging event remain unclear. With deeper X-ray observation of A209 in the future, the ICM properties and dynamical status of A209 could be better understood.

Acknowledgments

We extend our sincere appreciation to the anonymous referee for those comprehensive and valuable recommendations. This work is supported by the National Natural Science Foundation of China (grant Nos. U2038104 and 11703014) and the Bureau

of International Cooperation, Chinese Academy of Sciences (GJHZ1864).

ORCID iDs

Wen-Cheng Feng https://orcid.org/0000-0002-5484-6613
Heng Yu https://orcid.org/0000-0001-8051-1465
Hai-Hui Zhao https://orcid.org/0000-0001-7920-1486
Shu-Mei Jia https://orcid.org/0000-0002-5203-8321
Cheng-Kui Li https://orcid.org/0000-0001-5798-4491
Paolo Tozzi https://orcid.org/0000-0003-3096-9966
Ming Sun https://orcid.org/0000-0001-5880-0703

References

Annunziatella, M., Mercurio, A., Biviano, A., et al. 2016, A&A, 585, A160
Baba, H., Yasuda, N., Ichikawa, S.-I., et al. 2002, RNAOJ, 6, 23
Clowe, D., Bradač, M., Gonzalez, A. H., et al. 2006, ApJL, 648, L109
Dawson, W. A., Wittman, D., Jee, M. J., et al. 2012, ApJL, 747, L42
Ebeling, H., Voges, W., Bohringer, H., et al. 1996, MNRAS, 281, 799
Giovannini, G., Feretti, L., Govoni, F., Murgia, M., & Pizzo, R. 2006, AN, 327, 563
Haines, C. P., Mercurio, A., Merluzzi, P., et al. 2004, A&A, 425, 783
Knowles, K., Cotton, W. D., Rudnick, L., et al. 2022, A&A, 657, A56
Kravtsov, A. V., & Borgani, S. 2012, ARA&A, 50, 353
Lyskova, N., Churazov, E., Zhang, C., et al. 2019, MNRAS, 485, 2922
Mann, A. W., & Ebeling, H. 2012, MNRAS, 420, 2120
Maughan, B. J., Jones, C., Forman, W., & Speybroeck, L. V. 2008, ApJS, 174, 117
Menanteau, F., Hughes, J. P., Sifón, C., et al. 2012, ApJ, 748, 7
Mercurio, A., Girardi, M., Boschin, W., Merluzzi, P., & Busarello, G. 2003a, A&A, 397, 431
Mercurio, A., Massarotti, M., Merluzzi, P., et al. 2003b, A&A, 408, 57
Merten, J., Coe, D., Dupke, R., et al. 2011, MNRAS, 417, 333
Mirakhor, M. S., Walker, S. A., & Runge, J. 2023, MNRAS, 522, 2105
Paulin-Henriksson, S., Antonuccio-Delogu, V., Haines, C. P., et al. 2007, A&A, 467, 427
Planck Collaboration, Aghanim, N., Akrami, Y., et al. 2021, A&A, 652 C4
Postman, M., Coe, D., Benítez, N., et al. 2012, ApJ, 199, 25
Rossetti, M., Gastaldello, F., Ferioli, G., et al. 2016, MNRAS, 457, 4515
Sanders, J. S. 2006, MNRAS, 371, 829
Sasaki, T., Matsushita, K., Sato, K., & Okabe, N. 2016, PASJ, 68, 85
Sayers, J., Czakon, N. G., Mantz, A., et al. 2013, ApJ, 768, 177
Schellenberger, G., Reiprich, T. H., Lovisari, L., Nevalainen, J., & David, L. 2015, A&A, 575, A30
Seppi, R., Comparat, J., Nandra, K., et al. 2023, A&A, 671, A57
Shitanishi, J. A., Pierpaoli, E., Sayers, J., et al. 2018, MNRAS, 481, 749
Smith, G. P., Kneib, J.-P., Smail, I., et al. 2005, MNRAS, 359, 417
Smith, R. K., Brickhouse, N. S., Liedahl, D. A., & Raymond, J. C. 2001, ApJL, 556, L91
Venturi, T., Giacintucci, S., Brunetti, G., et al. 2007, A&A, 463, 937
Vikhlinin, A. A., Kravtsov, A. V., Markevich, M. L., Sunyaev, R. A., & Churazov, E. M. 2014, PhyU, 57, 317
von der Linden, A., Allen, M. T., Applegate, D. E., et al. 2014, MNRAS, 439, 2
Wen, Z. L., & Han, J. L. 2013, MNRAS, 436, 275
Yu, H., Tozzi, P., van Weeren, R., et al. 2018, ApJ, 853, 100
Zhang, Y. Y., Finoguenov, A., Böhringer, H., et al. 2007, A&A, 467, 437
Zhao, H.-H., Li, C.-K., Chen, Y., Jia, S.-M., & Song, L.-M. 2015, ApJ, 799, 47